

# Discovery of New Retrograde Substructures: The Shards of $\omega$ Centauri?

G. C. Myeong<sup>1\*</sup>, N. W. Evans<sup>1</sup>, V. Belokurov<sup>1</sup>, J.L. Sanders<sup>1</sup>, S.E. Koposov<sup>1,2</sup>

<sup>1</sup>*Institute of Astronomy, University of Cambridge, Madingley Road, Cambridge CB3 0HA*

<sup>2</sup>*McWilliams Center for Cosmology, Department of Physics, Carnegie Mellon University, 5000 Forbes Avenue, Pittsburgh, PA 15213, USA*

version 3 July 2018.

## ABSTRACT

We use the SDSS-*Gaia* catalogue to search for substructure in the stellar halo. The sample comprises 62 133 halo stars with full phase space coordinates and extends out to heliocentric distances of  $\sim 10$  kpc. As actions are conserved under slow changes of the potential, they permit identification of groups of stars with a common accretion history. We devise a method to identify halo substructures based on their clustering in action space, using metallicity as a secondary check. This is validated against smooth models and numerical constructed stellar halos from the Aquarius simulations. We identify 21 substructures in the SDSS-*Gaia* catalogue, including 7 high significance, high energy and retrograde ones.

We investigate whether the retrograde substructures may be material stripped off the atypical globular cluster  $\omega$  Centauri. Using a simple model of the accretion of the progenitor of the  $\omega$  Centauri, we tentatively argue for the possible association of up to 5 of our new substructures (labelled Rg1, Rg3, Rg4, Rg6 and Rg7) with this event. This sets a minimum mass of  $5 \times 10^8 M_{\odot}$  for the progenitor, so as to bring  $\omega$  Centauri to its current location in action – energy space. Our proposal can be tested by high resolution spectroscopy of the candidates to look for the unusual abundance patterns possessed by  $\omega$  Centauri stars.

**Key words:** galaxies: kinematics and dynamics – galaxies: structure

## 1 INTRODUCTION

The spatial structure of the stellar halo has already been explored using either multiband photometry from surveys like the Sloan Digital Sky Survey and Pan-STARRS (e.g., Belokurov et al. 2006; Bell et al. 2008; Slater et al. 2014) or variable stars such as RR Lyrae characteristic of old metal-poor stellar populations (Watkins et al. 2009; Iorio et al. 2018). At least within heliocentric distances of  $\sim 30$  kpc and for declinations northward of  $\delta = -30^{\circ}$ , the most prominent halo substructures in resolved star density maps have now been identified by matched filter searches (Newberg & Carlin 2015).

Nowadays, we are so familiar with maps such as the “Field of Streams” (Belokurov et al. 2006) that we forget how surprising they really are. Substructure identification in configuration space is grossly inefficient compared to searches in phase space (Johnston 1998; Helmi & White 1999). Streams remain kinematically cold and identifiable as substructure in phase space long after they have ceased to be recognisable in star counts against the stellar background of the galaxy. Given what has already been discovered with multiband photometry, the local phase space structure of the stellar halo must be bristling with abundant substructure.

Astrometric satellites have the ability to transform this terrain.

Already using data from the *Hipparcos* satellite, Helmi & White (1999) identified 13 stars which form an outlier in the plane defined by two components of angular momentum (see also Myeong et al. 2018a, for later developments). The first *Gaia* data release (DR1) in 2016 has already inspired two such searches. Helmi et al. (2017) used the Tycho-*Gaia* Astrometric Solution (TGAS) cross-matched with RAVE (Kunder et al. 2017) to identify overdensities in “integrals of the motion space”, or energy and angular momentum space, which they ascribed to halo substructure. Myeong et al. (2017) used TGAS cross-matched with RAVE-on (Casey et al. 2017) to search for halo substructure in action space, identifying a subset of stars with large radial action. These stars are all moving on highly eccentric orbits and are clustered in both configuration space and metallicity, thus providing a convincing candidate.

Crossmatches between TGAS and radial velocity surveys provide catalogues of  $\sim 2000$  halo stars largely within  $\sim 1$  kpc of the Sun. This is too parochial for studies of the stellar halo. The SDSS-*Gaia* catalogue contains a much larger and deeper sample of  $\sim 60\,000$  halo stars out to  $\sim 10$  kpc. This catalogue was made by recalibrating the Sloan Digital Sky Survey (SDSS) astrometric solution, and then obtaining proper motions from positions in the *Gaia* DR1 Source catalogue and their recalibrated positions in SDSS (see e.g., Deason et al. 2017; de Boer et al. 2018, for more details). The individual SDSS-*Gaia* proper motions have statistical errors typically  $\sim 2$  mas yr<sup>-1</sup>, or  $\sim 9.48D$  km s<sup>-1</sup> for a star with

\* E-mail: gm564,nwe,vasily,jls@ast.cam.ac.uk, koposov@cmu.edu

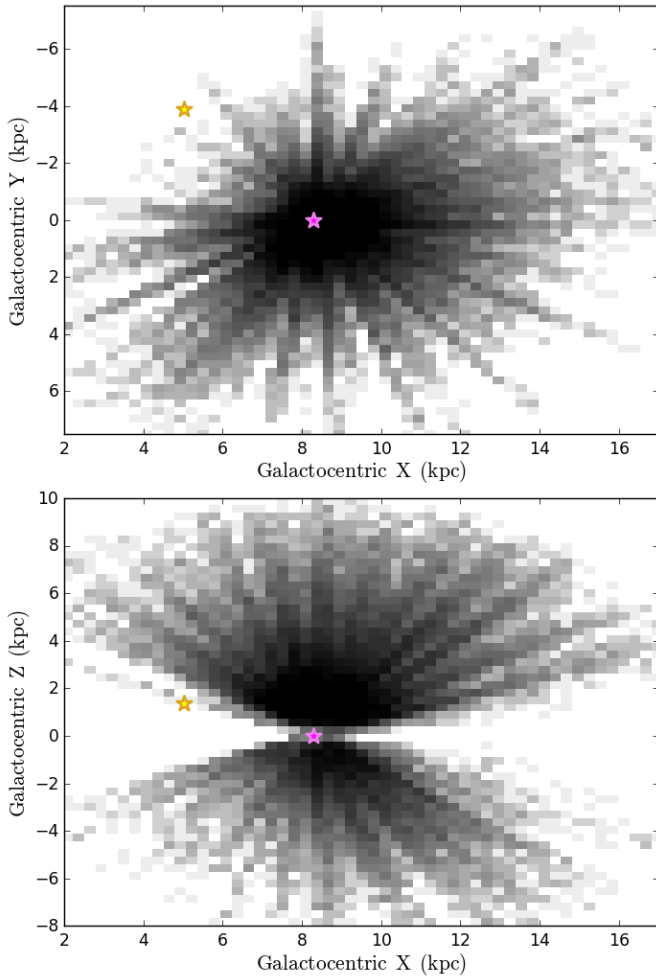


**Figure 1.** Distribution of the stellar halo sample in the SDSS-*Gaia* catalogue in spatial coordinates projected onto the principal planes ( $X, Y$ ) and ( $X, Z$ ) in Galactocentric Cartesian coordinates ( $X, Y, Z$ ). There are 62 133 halo stars with full phase space coordinates and the sample extends out to heliocentric distances of  $\sim 10$  kpc. The golden star in each panel represents the present position of  $\omega$  Centauri, while the mauve star is the position of the Sun. Note that  $\omega$  Centauri is at the low galactic latitude limit of the survey, so some of its debris may be missed.

heliocentric distance  $D$  kpc. The SDSS-*Gaia* catalogue is the natural intermediary between *Gaia* DR1 and the recently released *Gaia* DR2 (*Gaia Collaboration et al. 2018*).

*Myeong et al. (2018b)* recently provided new pictures of the Milky Way halo in action space as a function of metallicity using a sample of  $\sim 60\,000$  halo stars with full phase space coordinates present in the SDSS-*Gaia* catalogue. The comparatively metal-rich halo ( $-1.9 < [\text{Fe}/\text{H}] < -1.3$ ) is strongly retrograde at high energies (see e.g., Figure 2 of *Myeong et al. 2018b*). By contrast, at lower metallicities, there are very few halo stars that are retrograde and high energy. This is evidence of a considerable retrograde merger or accretion event in the recent past (e.g., *Quinn & Goodman 1986; Norris & Ryan 1989*).

Here, we carry out a search for halo substructure in action space using the SDSS-*Gaia* catalogue. This is a modification of our earlier search for halo substructure in velocity space (*Myeong et al. 2018a*). There are a number of advantages to using actions. Unlike integrals of motion, actions preserve their invariance under

slow changes (e.g., *Goldstein 1980*). They have often been suggested as the natural coordinates for galactic dynamics (see e.g., *Binney & Spergel 1982*), in which of course the potential is evolving in time. *Helmi & White (1999)* first argued that fossil structures in the stellar halo may be identifiable as clusters in action space. This idea has been tested extensively with numerical simulations both in static analytical potentials and in time-varying cosmological potentials (*Helmi & White 1999; Knebe et al. 2005; Gómez et al. 2010*).

The identification of substructures enables us to map out the accretion history of the Milky Way. For example, *Myeong et al. (2018a)* found two prominent substructures in velocity space (S1 and S2) and used a library of accreted remnants to estimate that they correspond to dwarf galaxies with virial masses of  $\approx 10^{10} M_{\odot}$  that fell into the Milky Way  $\gtrsim 9$  Gyr ago. Likewise, *Belokurov et al. (2018)* have suggested that the highly radially anisotropic velocity distribution of halo stars may be the imprint of a massive merger event, for which evidence also exists in the radial profile of the stellar halo density law (*Deason et al. 2013*).

Retrograde substructures are interesting, because they may be related to the anomalous globular cluster  $\omega$  Centauri. This has a present-day mass of  $5 \times 10^6 M_{\odot}$  (*Meylan et al. 1995*) and is believed to be the stripped nucleus of a dwarf galaxy (*Bekki & Freeman 2003*). This is bolstered by the fact that  $\omega$  Centauri has long been known to contain multiple stellar populations (*Norris et al. 1996; Suntzeff & Kraft 1996; Bedin et al. 2004*). Not merely do the stars in  $\omega$  Centauri exhibit a large metallicity spread (*Norris & Da Costa 1995*), but there are extreme star-to-star variations in many light elements (*Marino et al. 2012; Milone et al. 2017*). If  $\omega$  Centauri was once a dwarf galaxy, then its virial mass may have been as high as  $10^{10} M_{\odot}$  based on models of the chemical evolution of multi-population clusters (*Valcarce & Catelan 2011*). Dynamical evolutionary models find similar, though somewhat lower, starting values of  $\sim 10^8 - 10^9 M_{\odot}$  (e.g., *Bekki & Freeman 2003; Tsuchiya et al. 2003, 2004*). Therefore,  $\omega$  Centauri must have disgorged much of its initial mass of stars (and dark matter) as tidal debris in its passage to the inner Galaxy.

Searches for tidal debris in the solar neighbourhood date back to at least *Dinescu (2002)*, who found a retrograde signature in the solar neighbourhood for stars in the metallicity range  $-2.0 \leq [\text{Fe}/\text{H}] \leq -1.5$ . Further kinematic searches followed, though primarily with small samples of stars concentrated in the solar neighbourhood (e.g., *Mizutani et al. 2003; Brook et al. 2003; Meza et al. 2005; Fernández-Trincado et al. 2015*). *Majewski et al. (2012)* examined the line of sight velocities of  $\sim 3000$  metal-poor stars within 5 kpc and conjectured that most of the retrograde stars in the inner halo may be related to the disruption of  $\omega$  Centauri. There have also been suggestions of evidence of material torn from  $\omega$  Centauri by *Morrison et al. (2009)* and *Helmi et al. (2017)* based on their studies with 246 metal-poor stars and 1912 halo stars respectively. However, some specific groups that have been suggested as likely contenders for material stripped off – such as Kapteyn’s Moving Group (*Wylie-de Boer et al. 2010*) and the so-called  $\omega$  Centauri Moving Group (*Meza et al. 2005*) – have not survived detailed scrutiny based on the chemical evidence (*Navarrete et al. 2015*).

This paper is organised as follows. Section 2 describes our algorithm for substructure search in action space using the SDSS-*Gaia* catalogue. We identify 21 substructures in total with coherent kinematics and narrow metallicity distributions. Remarkably, we find that some of the most significant substructures are comparatively metal-rich, high energy and retrograde. Section 3 describes the properties of our retrograde candidates, and uses simple mod-

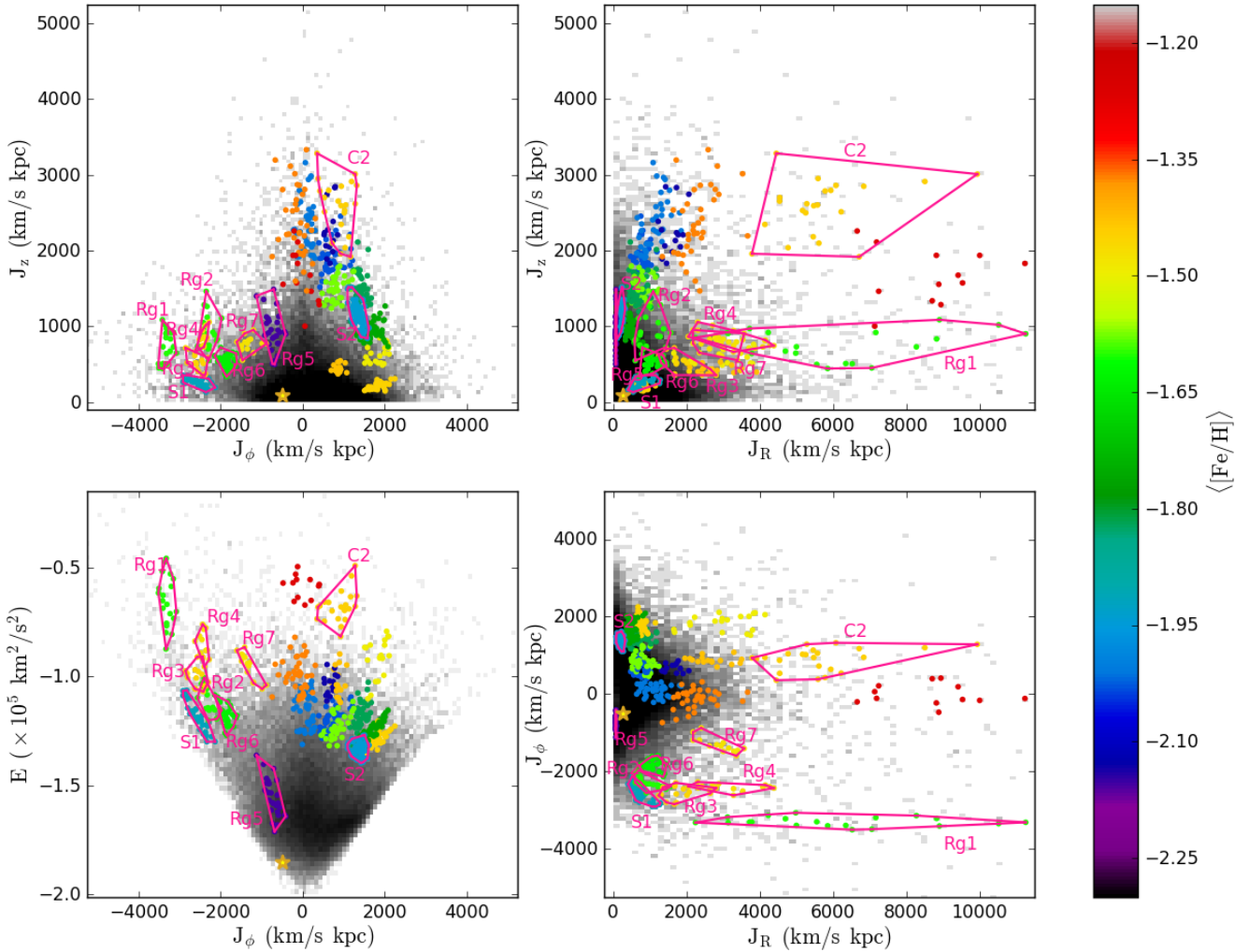


**Figure 2.** Distribution of the stellar halo sample and substructure candidates in action – energy space. Top left:  $(J_\phi, J_z)$ . Top right:  $(J_z, J_R)$ . Bottom left:  $(J_\phi, E)$ . Bottom right:  $(J_R, J_\phi)$ . The 21 most significant substructures are colour-coded according to metallicity. Previously found substructures (S1, S2, C2) and seven highlighted candidates (Rg1 – Rg7) are further highlighted with a magenta outline. The golden star in each panel represents the present position of  $\omega$  Centauri.

els of dynamical friction to investigate whether at least some of the new retrograde substructures are likely to be the shards of  $\omega$  Centauri. We draw our conclusions in section 4.

## 2 DETECTION OF SUBSTRUCTURES

### 2.1 Method

We use the SDSS-*Gaia* catalogue. This is created by the cross-match between *Gaia* data release 1 (DR1), the Sloan Digital Sky Survey data release 9 and LAMOST data release 3 (see, Ahn et al. 2012; Luo et al. 2015). Briefly, the main sequence turn-off stars (MSTOs) are extracted using the cuts: extinction  $\epsilon_r < 0.5$ ,  $g, r, i$  magnitudes satisfying  $14 < g < 20$ ,  $14 < r < 20$ ,  $14 < i < 20$ ,  $0.2 < (g - r)_0 < 0.8$  with surface gravity  $3.5 < \log g < 5.0$  and effective temperature  $4500 < T_{\text{eff}} < 8000$ . The rationale for the cuts is described in detail in Williams et al. (2017). The blue horizontal branch stars (BHBs) are chosen from  $-0.25 < (g - r)_0 < 0.0$ ,  $0.9 < (u - g)_0 < 1.4$  with spectroscopic parameters satisfying  $3.0 < \log g < 3.5$  and  $8300 < T_{\text{eff}} < 9300$ . Photometric par-

allaxes based on the SDSS photometry are used for MSTOs and BHBs using the formulae in Ivezić et al. (2008) and in Deason et al. (2011) to give full six-dimensional phase space coordinates. We apply a series of quality cuts to both the photometric and spectroscopic data to remove stars with poor measurements as well as stars with a heliocentric radial velocity error  $> 15$  km s $^{-1}$ , distance error  $> 2.5$  kpc, and a heliocentric distance  $> 10$  kpc.

We then convert the observables to velocities in the Galactic rest-frame. We use the Milky Way potential of McMillan (2017), which gives the circular speed at the Sun as 232.8 km s $^{-1}$ . For the Solar peculiar motion, we use the most recent value from Schönrich et al. (2010), namely  $(U, V, W) = (11.1, 12.24, 7.25)$  km s $^{-1}$ . The separation between the disk and the halo stars is carried out based on their azimuthal velocity and their metallicity (e.g., Myeong et al. 2018a). The equation for the excision of disk stars is

$$[\text{Fe}/\text{H}] \gtrsim -0.002 v_\phi - 0.9 \quad (1)$$

where  $v_\phi$  is the azimuthal velocity in direction of the Milky Way rotation and  $[\text{Fe}/\text{H}]$  the metallicity. This equation gives a good description of the more elaborate statistical separation displayed in Figure 1 of Myeong et al. (2018a). After the cuts, we obtain a sam-

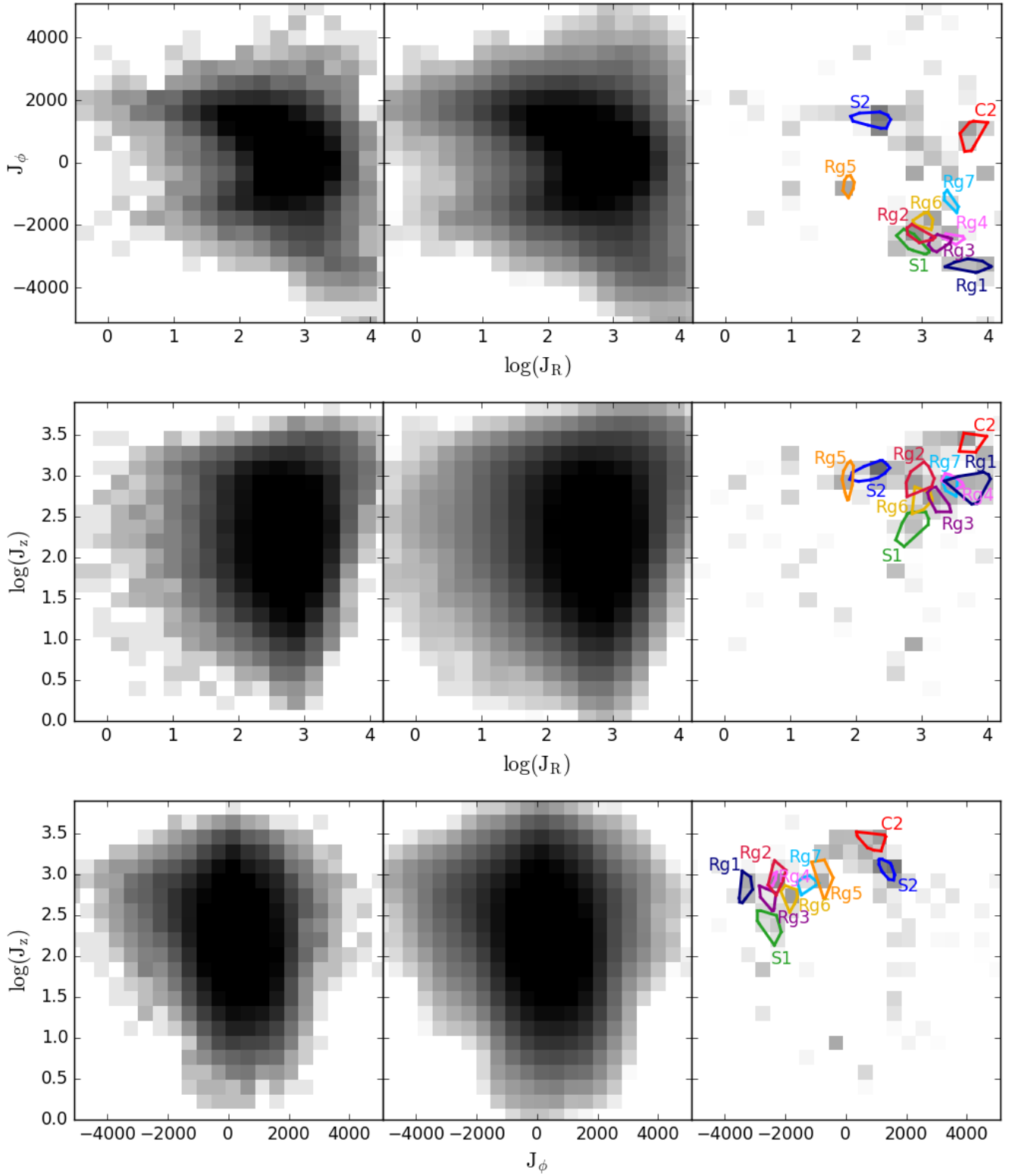


**Figure 3.** Two-dimensional projection of the detection space. We show from left to right the data, the smooth Gaussian kernel density model, and the residuals. The rows show the principal planes in action space  $(\log J_R, J_\phi)$ ,  $(\log J_R, \log J_z)$  and  $(J_\phi, \log J_z)$  respectively. Reassuringly, the residuals correspond to the locations of the main pieces of substructure.

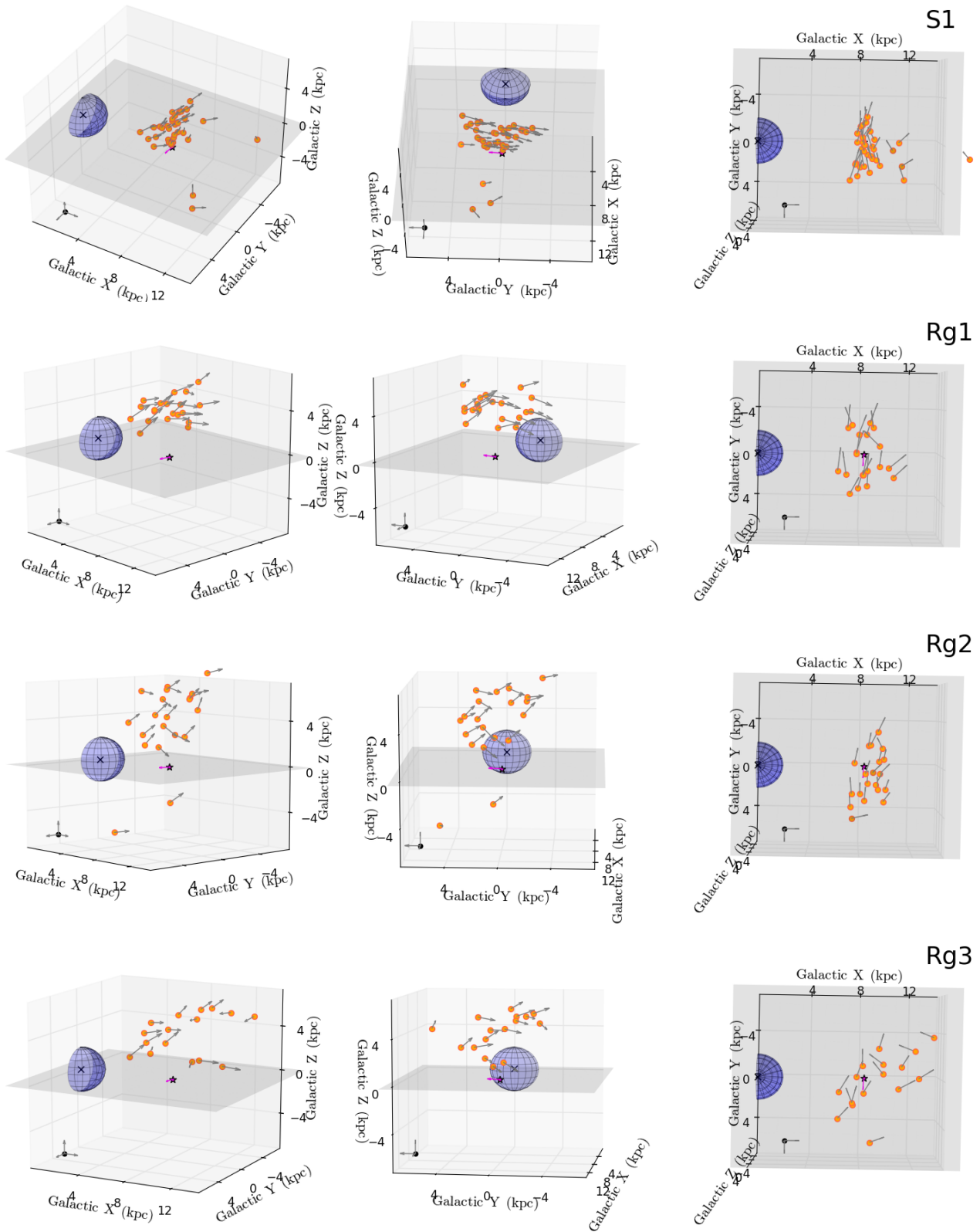


**Figure 4.** Spatial distribution of 4 selected retrograde substructures, the previously known S1 and the new Rg1, Rg2, and Rg3. Left and Middle: Two views of the substructure depicting the overall shape and motion. Right: Projection of the substructure onto the Galactic plane. The arrow shows the total Galactocentric velocity. The Sun and the Sun's motion are marked as a star and a magenta arrow. A 2 kpc radius sphere and a grey plane are crude representation of the Galactic bulge and the Galactic plane to give a sense of substructure's scale and location in Galactic frame. A black triad of velocity vectors (scale of  $300 \text{ km s}^{-1}$ ) is marked in each panel.



**Table 1.** The mean, mean absolute deviation and dispersions in positional and kinematic properties of the already known S1 and 7 new retrograde candidate substructures (Rg1 – Rg7). Also given are metallicity [Fe/H], as well as orbital properties, including energy  $E$ , circularity  $\eta$  (or ratio of total angular momentum to the angular momentum of a circular orbit of the same energy), and orbital inclination  $i$ . An electronic list of substructure member stars is available from the authors.

Name		[Fe/H]	$(J_R, J_\phi, J_z)$ ( $\text{kms}^{-1}\text{kpc}$ )	$\eta$	incl. $i$ (deg)	$(X, Y, Z)$ (kpc)	$(v_R, v_\phi, v_z)$ ( $\text{kms}^{-1}$ )	E ( $\text{km}^2\text{s}^{-2}$ )	Mem. no.
S1	Mean	-1.91	(749.7,-2551.1,253.4)	0.74	157.43	(8.9,0.6,2.5)	(-8.6,-286.7,-67.9)	-118958	34
	MAD	0.22	(186.6,180.9,51.2)	0.04	2.25	(1.0,1.2,1.2)	(104.5,40.9,45.8)	5761	
	Dispersion	0.26	(234.8,210.4,60.3)	0.05	2.56	(1.6,1.4,1.9)	(115.3,49.9,60.0)	6933	
Rg1	Mean	-1.60	(6066.6,-3309.0,759.5)	0.36	145.37	(8.3,0.2,4.3)	(54.1,-393.8,68.3)	-65634	20
	MAD	0.14	(2033.8,94.2,174.8)	0.08	3.94	(0.8,1.7,0.8)	(121.8,37.2,135.7)	9459	
	Dispersion	0.17	(2452.3,116.3,197.0)	0.09	4.54	(1.1,1.9,1.0)	(147.2,45.7,149.4)	11260	
Rg2	Mean	-1.60	(980.5,-2307.8,930.0)	0.71	136.29	(8.8,0.8,4.0)	(47.8,-254.6,71.8)	-109787	20
	MAD	0.12	(270.5,109.3,175.2)	0.05	3.56	(0.7,1.7,2.4)	(91.5,22.6,149.4)	6027	
	Dispersion	0.11	(303.1,140.8,221.0)	0.06	4.47	(0.8,2.0,3.2)	(110.2,27.8,172.1)	6578	
Rg3	Mean	-1.46	(1844.3,-2550.5,503.5)	0.54	148.35	(9.3,0.1,4.2)	(28.0,-275.1,18.0)	-99899	16
	MAD	0.17	(356.7,136.6,90.4)	0.05	3.01	(1.8,1.9,1.4)	(160.4,54.6,123.2)	3978	
	Dispersion	0.22	(445.8,163.5,112.2)	0.07	3.52	(2.1,2.3,1.6)	(186.0,62.7,136.5)	4769	
Rg4	Mean	-1.47	(3228.6,-2423.1,850.8)	0.42	138.64	(8.2,1.7,5.0)	(177.6,-287.9,117.9)	-84803	13
	MAD	0.14	(683.5,64.8,89.8)	0.06	2.40	(1.1,1.5,1.4)	(88.5,35.5,142.1)	5541	
	Dispersion	0.19	(781.9,85.2,111.4)	0.07	3.03	(1.6,1.8,1.7)	(114.6,46.0,162.7)	6217	
Rg5	Mean	-2.16	(75.4,-723.5,937.4)	0.89	114.98	(8.2,0.3,1.7)	(-10.0,-82.3,-0.6)	-155848	29
	MAD	0.23	(5.7,124.9,188.6)	0.02	3.71	(0.8,1.1,2.1)	(72.3,17.2,158.2)	7073	
	Dispersion	0.20	(7.2,154.4,247.1)	0.03	4.68	(1.1,1.4,3.0)	(83.2,21.2,162.7)	8588	
Rg6	Mean	-1.63	(1074.5,-1837.7,522.9)	0.60	141.76	(8.2,0.7,3.0)	(-11.9,-222.1,88.0)	-117935	30
	MAD	0.17	(174.0,94.8,74.4)	0.04	2.96	(1.4,1.3,2.0)	(178.6,35.4,115.1)	3336	
	Dispersion	0.22	(210.2,125.2,91.4)	0.05	3.72	(2.0,1.7,2.5)	(187.6,44.0,134.9)	4439	
Rg7	Mean	-1.48	(2883.7,-1314.8,770.6)	0.33	129.61	(8.6,0.1,4.4)	(-92.3,-160.2,-33.4)	-95342	14
	MAD	0.17	(385.4,148.8,70.7)	0.02	3.24	(1.6,1.1,2.0)	(255.2,53.2,138.0)	5236	
	Dispersion	0.24	(447.6,190.7,96.6)	0.03	4.07	(2.0,1.4,2.6)	(274.6,66.5,178.1)	6073	

ple of 62 133 halo stars comprising 61 911 MSTO stars and 222 BHB stars (59 811 stars with SDSS DR9 and 2 322 stars with LAMOST DR3 spectroscopy). The locations of these stars are shown projected onto the principal planes of the Galaxy in Fig. 1. Notice that the sample extends well beyond the solar neighbourhood out to heliocentric distances of 10 kpc. There are clear spatial selection effects, and the footprint of the Sloan Digital Sky Survey can be readily discerned. Nonetheless, the sample is kinematically unbiased and has already proved to be a treasure trove for substructure searches in velocity space (Myeong et al. 2018a).

Next, the actions of each star are computed using the numerical method of Binney (2012) and Sanders & Binney (2016). We construct a background model representing the underlying smooth distribution of the data in the 3-dimensional action space ( $\log(J_R), J_\phi, \log(J_z)$ ). We perform our search in logarithmic scale for  $J_R$  and  $J_z$  to compensate for the increase in spread of  $J_R$  and  $J_z$  which can reach large values for halo stars (see e.g., Figure 7 of Sanderson et al. 2015). The density estimation with a Gaussian kernel (KDE) from Scikit-learn (Pedregosa et al. 2011) is used with the optimal bandwidth determined by cross-validation. From this model, we generate 200 random samples with the same size as the data. For each sampling, we use a  $k$ -nearest neighbour search with  $k = 5$  to measure the density at the location of each star in the actual data. The mean of these 200 independent measurements is considered as the local density  $S_0$  expected by the model (compu-

tationally faster than deriving the model density by Gaussian KDE itself). The similar  $k$ -nearest neighbours search is applied on the original data to obtain the actual measured density  $S$ . From the probability density function,  $P(S) \approx S^{-k-1} \exp(-kS_0/S)$ , we compute the probability percentile of the measured density and convert it to the number of sigma indicating the significance.

Stars with significance  $> 4$  are used as “seeds” for searching for overdensities in action space. The seeds are first classified into several groups based on their relative location in the action space by the hierarchical agglomerative clustering implementation in Scikit-learn. For each seed, we collect nearby stars within a local volume of ellipsoid with semi-axes corresponding to one third of the standard deviation of each action. We discard any seeds that have less than 5 stars within this volume. The collected stars are classified by the Nearest Neighbours Classification from Scikit-learn. The classifier is trained on the pre-classified seeds and performs a distance-weighted ( $k = 3$ ) neighbours classification on stars. This provides us with a list of substructure candidates.

For each candidate, we measure the volume of ellipsoid in action space occupied by its member. The expected density (predicted by the model) at the centre of this volume is used to estimate the expected number of stars for the candidate, and hence obtain the significance (using the same method as described above). To obtain a high quality list, we require that a candidate (i) has significance  $> 4$ , (ii) contains more than 10 stars and (iii) has a metallicity dis-

**Table 2.** The mean, mean absolute deviation and dispersions in positional and kinematic properties of the prograde or radial candidate substructures. This includes the previously known S2 and C2, as well as the new candidates (Cand8 – Cand18). Also given are metallicity [Fe/H], as well as orbital properties, including energy  $E$ , circularity  $\eta$  (or ratio of total angular momentum to the angular momentum of a circular orbit of the same energy), and orbital inclination  $i$ . A list of substructure member stars is available from the authors electronically.

Name		[Fe/H]	$(J_R, J_\phi, J_z)$ ( $\text{kms}^{-1}\text{kpc}$ )	$\eta$	incl. $i$ (deg)	$(X, Y, Z)$ (kpc)	$(v_R, v_\phi, v_z)$ ( $\text{kms}^{-1}$ )	$E$ ( $\text{km}^2\text{s}^{-2}$ )	Mem. no.
S2	Mean	-1.94	(206.1,1363.3,1144.6)	0.88	58.64	(9.1,0.3,0.9)	(-11.2,159.6,-166.5)	-133500	73
	MAD	0.19	(45.6,101.2,118.8)	0.02	2.33	(1.0,0.9,2.6)	(46.7,16.6,110.7)	2488	
	Dispersion	0.23	(55.8,120.0,146.5)	0.03	2.96	(1.5,1.2,3.2)	(65.6,21.9,151.7)	2987	
C2	Mean	-1.45	(5718.7,896.5,2577.4)	0.30	75.55	(9.0,-0.6,2.3)	(-242.4,109.9,180.7)	-67927	22
	MAD	0.11	(938.3,247.9,282.7)	0.03	3.66	(0.9,0.8,1.9)	(155.1,28.5,189.5)	4916	
	Dispersion	0.13	(1359.0,296.6,354.3)	0.04	4.45	(1.2,0.9,2.5)	(229.2,35.9,236.1)	7011	
Cand8	Mean	-1.76	(498.5,1695.6,940.0)	0.77	51.72	(9.3,0.2,1.9)	(8.2,192.0,-25.0)	-125103	49
	MAD	0.21	(92.3,162.7,84.4)	0.03	2.01	(1.6,1.9,3.6)	(104.4,32.9,169.6)	3537	
	Dispersion	0.22	(117.4,197.9,109.0)	0.04	2.60	(2.0,2.4,4.2)	(124.0,40.2,186.6)	4317	
Cand9	Mean	-1.82	(672.2,1423.6,1488.1)	0.75	61.75	(9.1,-0.1,1.7)	(48.4,164.5,-171.1)	-118088	44
	MAD	0.15	(182.1,101.2,150.0)	0.04	1.90	(0.9,1.2,2.5)	(118.3,18.0,125.1)	4324	
	Dispersion	0.18	(221.4,123.2,201.3)	0.05	2.40	(1.2,1.6,3.4)	(139.6,24.2,172.0)	5626	
Cand10	Mean	-2.01	(1127.1,94.2,2345.9)	0.61	88.01	(8.7,0.0,1.8)	(-115.6,17.4,169.3)	-115259	39
	MAD	0.13	(255.7,123.3,269.8)	0.04	2.73	(1.4,1.0,2.0)	(175.1,15.1,137.8)	6958	
	Dispersion	0.18	(306.7,144.5,329.2)	0.06	3.23	(1.9,1.3,2.8)	(200.3,18.5,197.5)	7929	
Cand11	Mean	-2.03	(795.4,722.1,1903.9)	0.69	74.93	(9.1,-0.2,2.5)	(-82.8,91.7,41.4)	-119169	37
	MAD	0.20	(113.3,181.1,139.5)	0.04	2.68	(1.7,0.9,2.5)	(153.8,26.0,221.2)	4128	
	Dispersion	0.13	(144.3,222.8,185.1)	0.04	3.33	(2.1,1.2,3.2)	(171.1,36.6,239.8)	4980	
Cand12	Mean	-1.57	(800.8,828.0,1505.6)	0.66	70.26	(9.6,-0.8,3.7)	(-33.3,94.4,60.9)	-122892	36
	MAD	0.17	(174.1,152.3,129.1)	0.05	2.46	(1.6,2.1,3.2)	(151.8,21.9,173.4)	4141	
	Dispersion	0.19	(204.5,197.8,153.0)	0.06	3.01	(2.0,2.5,4.2)	(175.4,26.8,197.5)	5021	
Cand13	Mean	-1.37	(2272.7,-125.6,2356.9)	0.44	92.40	(9.1,1.0,3.1)	(-101.3,-9.3,98.4)	-98737	36
	MAD	0.13	(360.1,183.8,373.0)	0.04	3.71	(1.9,1.6,3.2)	(223.1,22.0,203.0)	5956	
	Dispersion	0.18	(481.6,239.5,449.8)	0.06	4.88	(2.5,2.0,4.1)	(246.4,30.4,238.1)	7373	
Cand14	Mean	-1.45	(777.4,1837.4,219.4)	0.65	30.97	(11.5,0.2,1.6)	(-51.6,170.5,-7.5)	-128409	36
	MAD	0.15	(91.2,130.2,37.5)	0.04	1.36	(1.6,1.4,3.1)	(155.1,20.9,79.9)	2408	
	Dispersion	0.17	(116.0,169.3,44.3)	0.05	1.75	(1.9,1.8,3.6)	(166.6,27.0,90.1)	3050	
Cand15	Mean	-1.49	(3041.5,1850.1,625.0)	0.37	43.60	(10.4,0.8,3.4)	(-73.6,186.4,-29.2)	-91662	19
	MAD	0.09	(635.1,170.2,93.3)	0.05	2.17	(1.6,1.7,3.9)	(272.3,25.4,108.5)	6905	
	Dispersion	0.10	(760.4,195.2,108.6)	0.05	2.63	(1.9,2.3,4.8)	(285.9,34.7,129.2)	8796	
Cand16	Mean	-1.43	(2769.2,875.5,450.8)	0.25	50.53	(8.7,1.1,2.3)	(114.6,107.3,90.7)	-102594	17
	MAD	0.12	(450.5,66.2,44.9)	0.04	2.88	(1.2,1.6,3.8)	(255.8,15.6,122.5)	5501	
	Dispersion	0.09	(538.2,88.9,53.4)	0.05	3.57	(1.5,2.0,4.4)	(283.2,19.3,146.9)	6526	
Cand17	Mean	-2.13	(1614.4,673.3,2263.4)	0.56	77.22	(9.7,-0.3,2.6)	(29.0,77.5,116.5)	-103328	14
	MAD	0.15	(210.4,89.7,251.5)	0.03	1.40	(1.0,0.8,1.7)	(171.1,10.6,230.6)	4013	
	Dispersion	0.18	(240.2,101.4,317.8)	0.04	1.67	(1.3,0.9,2.5)	(201.1,13.2,269.9)	4778	
Cand18	Mean	-1.27	(8654.9,-18.1,1665.1)	0.14	89.88	(7.2,-0.1,5.3)	(-151.7,-8.3,-26.3)	-58877	12
	MAD	0.12	(1060.5,223.2,294.1)	0.02	6.96	(2.3,1.6,1.4)	(398.6,35.0,117.5)	4395	
	Dispersion	0.14	(1304.9,257.8,350.7)	0.03	8.00	(3.1,1.8,1.6)	(424.7,40.6,142.8)	5216	

tribution function (MDF) strongly peaked in comparison with the halo MDF. The latter is judged by first decomposing the halo MDF into two Gaussians (with dispersions 0.38 and 0.27 as the result of Gaussian mixture model. see e.g., Figure 1 of Myeong et al. 2018a). We require that a Gaussian fit to our candidate MDF should have a dispersion less than 0.27, ensuring that it is peakier than the halo MDF. This gives us 21 candidate substructures.

## 2.2 Algorithm Validation

Before proceeding, we report two cross-checks. Using the public software package AGAMA (Vasiliev 2018), we generated a smooth model of a stellar halo (Williams & Evans 2015) in the potential of McMillan (2017). We created a catalogue of 250 000 stars within a heliocentric distance of 10 kpc around the Sun with the disk and the bulge region eliminated using  $|z| > 1.5$  kpc and  $r > 3.0$  kpc. The algorithm identified no substructures as it found no “seeds”.

Secondly, we tested on publicly available stellar haloes created by cosmological zoom-in simulations. We used the Aquarius catalogue provided by [Lowing et al. \(2015\)](#). The catalogue lists the "TreeID" for each star providing the information of the parent satellite that brought the star into the main halo. We obtained the catalogue of 250 000 stars with 49 TreeIDs in the local volume of 10 kpc around the Sun with disk and bulge region excluded. However, some of the TreeIDs contribute very few stars in the local volume. There are 34 TreeIDs with  $> 50$  stars. This seems a reasonable figure against which to measure performance of our method.

Our algorithm identified 28 candidate substructures after applying the significance  $\sigma > 4$  and number of member stars  $> 10$  cuts. The smallest candidate has 40 stars. Although all the substructures identified by the algorithm are real, there is not a one-to-one correspondence between TreeIDs and candidates. Of these, 2 TreeIDs are detected as multiple candidates (4 candidates and 3 candidates respectively) and 2 candidates show significant internal blending of multiple TreeIDs. For the case of blended candidates, we note that these multiple TreeIDs in the same candidate have virtually the same actions. Interestingly, they also occupy the same region in the configuration space with the indistinguishable streaming motion – therefore the same actions. This may be a case of multiple satellites accreted to the main halo along the same dark matter filament at a similar redshift. In this case, multiple TreeID groups are accreted with almost identical kinematics.

We conclude that the present algorithm works well, in the sense of identifying overdensities with high significance and generating candidate lists for these overdensities. In particular, the tunable parameters in the algorithm (bandwidth, linking procedure, number of nearest neighbours) have been set conservatively. Although some highly disrupted structures are missed, most substructures get picked up, unless they are too small in size.

Our method has some points of similarity with [Helmi et al. \(2017\)](#) and also some points of difference, which it is useful to summarise. Both algorithms use the data to derive a smooth background model. However, our search proceeds in action space, whereas [Helmi et al. \(2017\)](#) use an 'integral of motion space' that is most appropriate for a spherical potential. Secondly, [Helmi et al. \(2017\)](#) begins with a two-dimensional search in  $(E, J_\phi)$  with a corroborating check for projections in the third integral of motion, whereas we carry out our search in the three-dimensional action space  $(J_R, J_\phi, J_z)$  from the beginning. Thirdly, [Helmi et al. \(2017\)](#) do not account for the Solar peculiar motion and take the Local Standard of Rest as  $220 \text{ km s}^{-1}$ , whereas we use the circular speed at the Sun as  $232.8 \text{ km s}^{-1}$  and the Solar peculiar motion from [Schönrich et al. \(2010\)](#), namely  $(U, V, W) = (11.1, 12.24, 7.25) \text{ km s}^{-1}$ . These differences are important, as for very local stars they can cause a change from prograde to retrograde. Fourthly, we require that the metallicity distribution functions of our substructures to be strongly peaked, whereas no such requirement is imposed in [Helmi et al. \(2017\)](#). These differences in methodology mean that we do not detect any of the "VelHels" identified by [Helmi et al. \(2017\)](#). Many of the "VelHels" have rather broad metallicity distribution functions ([Veljanoski & Helmi 2018](#)) and would fail our criteria.

Although the algorithms are related, the main difference is the size of the dataset through which we search. [Helmi et al. \(2017\)](#) uses a sample of 1912 halo stars extracted from TGAS cross-matched with RAVE. Our algorithm has been applied to a sample of 62 133 stars with full six-dimensional phase space information in the SDSS-*Gaia* catalogue (see e.g., [Deason et al. 2017](#); [de Boer et al. 2018](#)). We identified 21 high significance substructures. These all have morphological features that resemble segments of orbits

close to pericentre, as well as compact metallicity distributions. The stars belonging to the substructures are therefore kinematically and chemically similar.

### 3 SUBSTRUCTURE FORENSICS

[Fig. 2](#) shows the 21 high significance substructures in action space and integral of motion space. The data, the underlying smooth model from the Gaussian kernel density estimator and the residuals are shown in the left, middle and right panels of [Fig. 3](#). Reassuringly, the identified substructures correspond to prominent residuals, mainly in the outer, relatively less dense parts of the distribution. This is an effect due to the imposition of high significance in candidate selection. Candidates detected at the central denser regions are more vulnerable to blending with random contaminants. Since we use compactness of the MDF of the candidates as one of the criteria for validation, it is natural for us to identify more substructures with high significance in less dense regions. Another thing to notice is that a significant number are in a retrograde tail of stars that emanates from the main body of the distribution in [Fig. 2](#). In fact, two of the top three most significant substructures are retrograde. The population of high energy retrograde stars provides a very happy hunting ground for halo substructure in general.

We list the properties of all the retrograde candidates in [Table 1](#). The table gives their mean locations, velocities in the Galactic rest-frame and metallicity. We also report their orbital properties, including mean energy  $E$  and circularity  $\eta$ , which is the ratio of total angular momentum to the angular momentum of a circular orbit of the same energy  $L/L_{\text{circ}}(E)$ . Another orbital quantity of interest is the inclination to the Galactic plane, defined as  $i = \arccos(J_\phi/J)$  where  $J$  is the absolute value of the total angular momentum. Although we do not study the new prograde substructure candidates in detail in this paper, we list their basic properties in [Table 2](#). Electronic tables of member stars are available from the authors.

#### 3.1 Cross-checks: Known Candidates (S1, S2, C2)

[Myeong et al. \(2018a\)](#) already identified six halo substructures in the SDSS-*Gaia* catalogue from a search in velocity space. Only three are recovered here with high significance, namely S1, S2 and C2. What happened to the remaining substructures? Two (S3, S4) are found, but at lower significance than we imposed here. C1 is also identified with a large portion of new members, but it fails the requirement that we insisted that the substructure have a compact metallicity distribution. The velocity-based search was more successful in recovering seemingly clean stream-like structures for S2 and C2. However, the power of action space is that it can associate patches of substructures from different pericentric passages ([Helmi & White 1999](#)). This means that more highly phase-mixed material can be associated with the substructure, and so we expect more disrupted morphologies.

#### 3.2 The Retrograde Candidates

These include the previously known S1, and the seven new retrograde candidates (Rg1–7, in order of decreasing significance). The morphology of some of the retrograde substructures is shown in [Fig. 4](#). Their shapes are strongly affected by the footprint, as the stars must lie in the SDSS so the coverage of the Southern Galactic hemisphere is patchy. Occasionally, there are stars that do not seem to agree with the overall morphology of the substructure (e.g., in



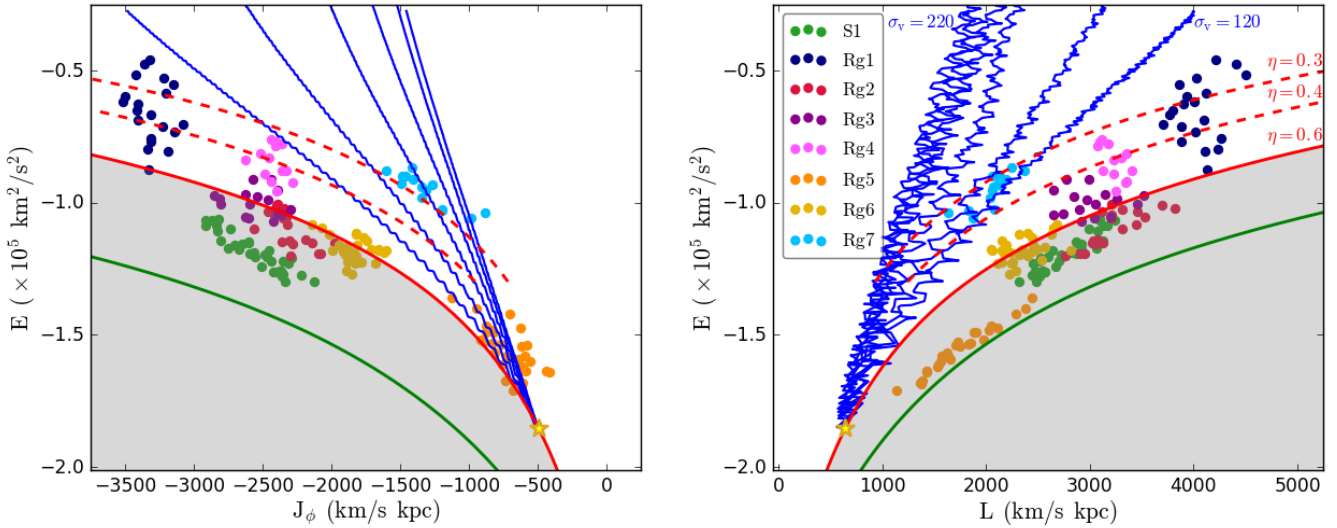


**Figure 5.** Orbital tracks of  $\omega$  Centauri in action space ( $E, J_\phi$ ) and ( $E, L$ ) as the progenitor sinks to its present location, together with the retrograde substructures (S1 and Rg1–7). The golden star marks the present position of  $\omega$  Centauri. The blue tracks the trajectory of the progenitor to the present-day  $\omega$  Centauri, as given by numerical integration assuming Chandrasekhar dynamical friction with the velocity dispersion of the dark matter varying from 120  $\text{km s}^{-1}$  to 220  $\text{km s}^{-1}$  in steps of 20  $\text{km s}^{-1}$ . We also show the evolution tracks of an object with a constant circularity  $\eta \approx 0.6$  (solid red line) corresponding to  $\omega$  Centauri today, whilst dashed red lines show further constant circularity tracks (0.4 and 0.3). The grey shaded area shows the range of locations in which tidally-torn streams may not reside, as  $\omega$  Centauri’s circularity cannot have diminished during its orbital evolution. The green lines mark the (retrograde) circular orbit limit.

Rg3 there are two stars whose velocity vectors run counter to the trends seen in the remaining stars in the arm). These could be contaminants, but they could also be phase-mixed material. Nonetheless, the overall shapes of the substructures, as well as their velocity distributions, are consistent with orbital segments close to pericentre. The candidates all share similar characteristics in that they are retrograde and all (but one) belong to Myeong et al. (2018b)’s categorisation of the comparatively metal-rich halo ( $-1.9 < [\text{Fe}/\text{H}] < -1.3$ ). They are tightly clustered in azimuthal action  $J_\phi$ , but typically have much larger spreads in  $J_R$  and  $J_z$ . It is interesting to compare S1 as selected in action space with the more ragged view of the same substructure as selected in velocity space and given in Figure 5 of Myeong et al. (2018a). This retrograde substructure passes right through the solar neighbourhood. If there is a dark matter stream associated with this substructure, then it may have important consequences for direct detection experiments.

Of course,  $\omega$  Centauri is known to be on a retrograde orbit. Its proper motion has recently been re-measured by Libralato et al. (2018) and differs somewhat from the previous value. Using the potential of McMillan (2017), the present energy of  $\omega$  Centauri is  $-1.85 \times 10^5 \text{ km}^2 \text{ s}^{-2}$ , whilst its actions ( $J_R, J_\phi, J_z$ ) are (264.5, -496.4, 93.5)  $\text{km s}^{-1} \text{ kpc}$ . Its position is marked as a golden star in the action plots of Fig. 2. This gives a total angular momentum of 646.62  $\text{km s}^{-1} \text{ kpc}$  and a present day circularity of  $\eta \approx 0.60$  for  $\omega$  Centauri. Usually, the effect of dynamical friction on orbits of moderate eccentricity is to circularize orbits. However, van den Bosch et al. (1999) find that the orbital circularity can sometimes stay roughly constant throughout the decay. The eccentricity decreases near the pericentre, but increases near the apocentre such that there is only mild net circularisation or radialisation in their simulations in an admittedly spherical potential (see Figure 9 of van den Bosch et al. 1999). It is reasonable to conjecture that the orbit of  $\omega$  Centauri can only get more circular with time, or – in this limiting case – stay constant. Thus, the circularity  $\eta = 0.6$  line is a limit below which it

is not sensible to associate substructure with  $\omega$  Centauri. This rules out S1, Rg2 and Rg5 as belonging to the sinking  $\omega$  Centauri.

The circularity  $\eta = 0.6$  line is shown in Fig 5 with the region below it shaded grey as forbidden. We also show the tracks in red for objects evolving with constant circularity of 0.4 and 0.5 in action space. In addition, we have supplemented these with blue tracks showing the simple model trajectory of an  $\omega$  Centauri progenitor (represented as a point mass of  $5 \times 10^8 M_\odot$ ) moving in the Galactic potential of McMillan (2017) and under the influence of dynamical friction as judged by the Chandrasekhar (1943) formula, with the velocity dispersion of the dark matter particles as 120  $\text{km s}^{-1}$  to 220  $\text{km s}^{-1}$  in 20  $\text{km s}^{-1}$  intervals (see also, Chapter 8.1 of Binney & Tremaine 2008). We use the factor  $\Lambda$  in the Coulomb logarithm from the equation (8.1b) in Binney & Tremaine (2008). We note that these tracks are simple model trajectories and although the Chandrasekhar formula can provide a good description for orbital decay under dynamical friction (Binney & Tremaine 2008), a more realistic picture will require more sophisticated methods such as N-body simulations (see also, Weinberg 1989; Fujii et al. 2006). Although we consider  $\omega$  Centauri as a point mass, its internal velocity dispersion could produce scatter about the tracks. Still, at  $5 \times 10^8 M_\odot$ , the scatter would have a modest effect on the overall direction of the trajectory. The rate of circularisation does depend on the choice of parameters, especially the velocity dispersion of the halo. These tracks are much steeper, but it is actually difficult to push the trajectories to lower values of  $J_\phi$  than that of the present day  $\omega$  Centauri. Of course, this calculation omits any effects due to mass loss from  $\omega$  Centauri or evolution of the Milky Way potential. Given that the structure of the progenitor and the workings of dynamical friction in the Galaxy are not well-known, we regard the region between the constant circularity line  $\eta = 0.60$  and the most extreme Chandrasekhar curve as the likely area in which tidal fragments are to be sought and found. This suggests that the substructures Rg1, Rg3, Rg4, Rg6 and Rg7 are all possible candidates.

Further evidence can be provided by the inclinations of the substructures, which are listed in Table 1. Here, we use the traditional convention that inclinations greater than  $90^\circ$  describe retrograde orbits. The effect of dynamical friction is to drag the orbit of a sinking satellite down towards the Galactic plane. Unsurprisingly  $\omega$  Centauri is now on a rather low inclination orbit  $i_{OC} = 140.15^\circ$ . So, candidates with more inclined retrograde orbits (that is, smaller  $i$ ), or within the range of their dispersion with the present day inclination of  $\omega$  Centauri, are feasible. Rg1 has a slightly less inclined orbit ( $i = 145.37^\circ$ ), but considering its dispersion of  $4.54^\circ$ , it is still plausible. Rg3 has a less inclined orbit ( $i = 148.35^\circ$ ), and even taking into account its dispersion, it does not cause it to overlap with  $i_{OC}$ . Rg4 has comparable but more inclined orbit ( $138.64^\circ$ ). Rg6 has a slightly less inclined orbit ( $141.76^\circ$ ), while its dispersion takes it within the range. Rg7 has considerably more inclined orbit ( $129.61^\circ$ ) – more than  $10^\circ$  difference. This leaves Rg1, Rg4, Rg6 as the strongest candidates, with Rg3 and Rg7 somewhat less favoured.

The validity of the claims can be established by seeing which substructures are chemically consistent with  $\omega$  Centauri via high resolution spectroscopy. Navarrete et al. (2015) studied two prominent pieces of retrograde substructure, Kapteyn’s Moving Group, and the so-called  $\omega$  Centauri group. Both have been previously been claimed to be material shed by  $\omega$  Centauri on its journey to the inner Galaxy (Meza et al. 2005; Wylie-de Boer et al. 2010). However, both groups are not related to  $\omega$  Centauri, based on abundances from Na, O, Mg, Al, Ca and Ba derived from optical spectra. In particular,  $\omega$  Centauri has characteristic Na-O and Mg-Al patterns of abundances for moderately metal-rich halo stars, as well as an overabundance of Ba, that are different from the halo field stars. The GALAH survey (Buder et al. 2018), with its range of elemental abundances, may also be useful here.

If the substructures are not related to  $\omega$  Centauri, then they are perhaps even more interesting and puzzling! Presumably they must then be the remnants of objects that are highly phase-mixed and so little now remains even of the nucleus. Studying the elemental abundance ratios of the retrograde substructure will greatly benefit the unravelling of their true origin. In particular, we would obtain evidence on the importance of rapid (r) and slow (s) process enrichment. It would be interesting to see if they show evidence for the anomalous r-process enhancement, already detected for some of the faintest dwarf galaxies (Ji et al. 2016; Roederer 2017). To this end, the authors happily make available electronic tables of the member stars in the retrograde substructures as target lists for spectroscopy.

#### 4 CONCLUSIONS

This paper has developed a new algorithm to search for substructure in action space. As actions are conserved under slow evolution of the potential, stars accreted onto the Milky Way halo in the same merger event should be clustered in action space. Thus, the algorithm searches for significant overdensities with respect to the data-derived background model. The metallicity distribution function of the substructures is required to be more strongly peaked than the stellar halo metallicity distribution function itself. The final substructure candidates are therefore clustered both in action and in metallicity. Our algorithm has been validated against mock catalogues of substructure in the Aquarius cosmological zoom-in simulations provided by Lowing et al. (2015).

This algorithm is similar in spirit to our earlier search strategy in velocity space, though here we have used a Kernel density

estimator to model the background rather than a Gaussian mixture model (Myeong et al. 2018a). We applied our algorithm to a sample of 62 133 halo stars with full phase space coordinates extracted from the SDSS-*Gaia* catalogue. The sample size is at least an order of magnitude greater than any previous substructure search in phase space (see e.g., Morrison et al. 2009; Helmi et al. 2017). The stars extend out to heliocentric distances of  $\sim 10$  kpc, and this permits us to identify coherent features in phase space in an unprecedentedly large volume of the Galaxy.

Altogether, we identified 21 high significance substructures in action space. Here, we have focussed on eight substructures that lie in the retrograde, high energy portion of action space. This includes the previously discovered S1 substructure (Myeong et al. 2018a), as well as seven new candidates (Rg1–7). Myeong et al. (2018b) already showed that the retrograde, high energy stars in the local halo are confined to a restricted range of metallicities ( $-1.9 < [\text{Fe}/\text{H}] < -1.3$ ). The origin of this high energy and clumpy component of the local stellar halo remains a puzzle. Although the substructure must have come from mergers of retrograde satellites, it remains unclear whether one large satellite or multiple smaller ones are responsible.

One possible source of the abundant retrograde substructure is the anomalous globular cluster,  $\omega$  Centauri. There is a long history of searches in the solar neighbourhood for stars tidally torn from  $\omega$  Centauri (e.g., Dinescu 2002; Meza et al. 2005; Morrison et al. 2009). On studying a sample of metal-poor halo giants within  $\sim 5$  kpc, Majewski et al. (2012) made the bold conjecture that the disruption of the progenitor of  $\omega$  Centauri may have generated a very substantial part of the retrograde population in the stellar halo. It is this hypothesis that we can hope to test with substructure searches in deeper halo catalogues like SDSS-*Gaia*.

Here, we have shown based on kinematic evidence that three of our substructures (Rg1, Rg4, Rg6) could be the shards of  $\omega$  Centauri. Rg3 and Rg7 are also possible, though they are somewhat disfavoured on the grounds of their present inclination. S1, Rg2 and Rg5 seem ruled out on the grounds of their present circularity. The timescale of the orbital decay due to the dynamical friction depends on the mass of the satellite (e.g. van den Bosch et al. 1999). Since this timescale must be shorter than a Hubble time, then, given the current energy and location of  $\omega$  Centauri, the progenitor must have had a mass of at least  $5 \times 10^8 M_\odot$ , comparable to the value found by Bekki & Freeman (2003). This sets a lower bound, as this is an average mass throughout the orbital decay over the Hubble time. Moreover, the mass loss from the tidal stripping and the evolution of the Milky Way potential could cause the actual initial mass to be greater by perhaps an order of magnitude (e.g., Tsuchiya et al. 2003).

The most direct way to test the claims of this paper is by obtaining high resolution spectroscopy of the candidate stars in the substructures. In particular,  $\omega$  Centauri has characteristic Na-O and Mg-Al patterns of abundances for moderately metal-rich halo stars, as well as an overabundance of Ba, that are different from the halo field stars (c.f. Navarrete et al. 2015). Furthermore, suppose for example we establish that Rg3 and Rg4 (but not the others) were associated with  $\omega$  Centauri. Then, this would provide significant constraints on the progenitor and the action of dynamical friction, as we would know whether the orbit is circularising. Another intriguing possibility is that the highest energy substructures may have been stripped before extended star formation and multiple population enrichment, and so it may even be possible to see gradients across the substructures.

If chemical evidence disproves our assertion that some of the

retrograde substructures belong to  $\omega$  Centauri, then the situation is perhaps even more interesting. It leaves us with two major puzzles. First, where are the substantial amounts of debris that must have been shed by the  $\omega$  Centauri progenitor? And second, what is the origin of the high energy, retrograde halo which is riven with substructure? The recent release of the Gaia DR2 dataset (Gaia Collaboration et al. 2018) offers further golden prospects for resolving these puzzles, as well as for harnessing the power of substructure identification algorithms to build a complete inventory of merger remnants in the stellar halo. The algorithms and techniques that we have developed here will have no small part to play.

## ACKNOWLEDGEMENTS

We thank the Cambridge Streams Group (especially Eugene Vasiliev) and Nicola Amorisco for helpful conversations. GCM thanks Boustany Foundation, Cambridge Commonwealth, European & International Trust and Isaac Newton Studentship for their support on his work. JLS thanks the Science and Technology Facilities Council for financial support. We are grateful to the anonymous referee who helped us improve this work. The research leading to these results has received partial support from the European Research Council under the European Union's Seventh Framework Programme (FP/2007-2013) / ERC Grant Agreement no. 308024.

## REFERENCES

Ahn, C. P., et al. 2012, *ApJS*, 203, 21  
 Bedin, L. R., Piotto, G., Anderson, J., et al. 2004, *ApJ*, 605, L125  
 Bekki, K., & Freeman, K. C. 2003, *MNRAS*, 346, L11  
 Belokurov, V., Zucker, D. B., Evans, N. W., et al. 2006, *ApJ*, 642, L137  
 Belokurov, V., Erkal, D., Evans, N. W., Koposov, S. E., & Deason, A. J. 2018, arXiv:1802.03414  
 Bell, E. F., Zucker, D. B., Belokurov, V., et al. 2008, *ApJ*, 680, 295-311  
 Binney, J. 2012, *MNRAS*, 426, 1324  
 Binney, J., & Spergel, D. 1982, *ApJ*, 252, 308  
 Binney, J., & Tremaine, S. 2008, *Galactic Dynamics*, 2nd edn. Princeton Univ. Press, Princeton, NJ  
 de Boer, T. J. L., Belokurov, V., & Koposov, S. E. 2018, *MNRAS*, 473, 647  
 Brook, C. B., Kawata, D., Gibson, B. K., & Flynn, C. 2003, *ApJ*, 585, L125  
 Buder, S., Asplund, M., Duong, L., et al. 2018, arXiv:1804.06041  
 Casey, A. R., Hawkins, K., Hogg, D. W., et al. 2017, *ApJ*, 840, 59  
 Chandrasekhar, S. 1943, *ApJ*, 97, 255  
 Deason, A. J., Belokurov, V., Evans, N. W., 2011, *MNRAS*, 416, 2903  
 Deason, A. J., Belokurov, V., Evans, N. W., & Johnston, K. V. 2013, *ApJ*, 763, 113  
 Deason, A. J., Belokurov, V., Koposov, S. E., et al. 2017, arXiv:1703.09230  
 Dinescu, D. I. 2002, *Omega Centauri, A Unique Window into Astrophysics*, 265, 365  
 Fernández-Trincado, J. G., Robin, A. C., Vieira, K., et al. 2015, *A&A*, 583, A76  
 Fujii, M., Funato, Y., Makino, J. 2006, *PASJ*, 58, 743  
 Gaia Collaboration, Brown, A. G. A., Vallenari, A., et al. 2018, arXiv:1804.09365  
 Goldstein, H., 1980, *Classical Mechanics*, Addison-Wesley  
 Gómez, F. A., Helmi, A., Brown, A. G. A., & Li, Y.-S. 2010, *MNRAS*, 408, 935  
 Helmi, A., & White, S. D. M. 1999, *MNRAS*, 307, 495  
 Helmi, A., Veljanoski, J., Breddels, M. A., Tian, H., & Sales, L. V. 2017, *A&A*, 598, A58  
 Iorio, G., Belokurov, V., Erkal, D., et al. 2018, *MNRAS*, 474, 2142  
 Ivezić, Z., et al. 2008, *ApJ*, 684, 287  
 Ji, A. P., Frebel, A., Chiti, A., & Simon, J. D. 2016, *Nature*, 531, 610  
 Johnston, K. V. 1998, *ApJ*, 495, 297

Kunder, A., Kordopatis, G., Steinmetz, M., et al. 2017, *AJ*, 153, 75  
 Knebe, A., Gill, S. P. D., Kawata, D., & Gibson, B. K. 2005, *MNRAS*, 357, L35  
 Libralato, M., Bellini, A., Bedin, L. R., et al. 2018, *ApJ*, 854, 45  
 Lowing, B., Wang, W., Cooper, A., et al. 2015, *MNRAS*, 446, 2274  
 Luo, A.-L., Zhao, Y.-H., Zhao, G., et al. 2015, *Research in Astronomy and Astrophysics*, 15, 1095  
 Majewski, S. R., Nidever, D. L., Smith, V. V., et al. 2012, *ApJ*, 747, L37  
 Marino, A. F., Milone, A. P., Piotto, G., et al. 2012, *ApJ*, 746, 14  
 McMillan, P. J. 2017, *MNRAS*, 465, 76  
 Meylan, G., Mayor, M., Duquennoy, A., & Dubath, P. 1995, *A&A*, 303, 761  
 Meza, A., Navarro, J. F., Abadi, M. G., & Steinmetz, M. 2005, *MNRAS*, 359, 93  
 Milone, A. P., Marino, A. F., Bedin, L. R., et al. 2017, *MNRAS*, 469, 800  
 Mizutani, A., Chiba, M., & Sakamoto, T. 2003, *ApJ*, 589, L89  
 Morrison, H. L., Helmi, A., Sun, J., et al. 2009, *ApJ*, 694, 130  
 Myeong, G. C., Evans, N. W., Belokurov, V., Koposov, S. E., & Sanders, J. L. 2017, *MNRAS*, 469, L78  
 Myeong, G. C., Evans, N. W., Belokurov, V., Amorisco, N., Koposov, S. E. 2018a, *MNRAS*, 475, 1537  
 Myeong, G. C., Evans, N. W., Belokurov, V., Sanders, J. L., & Koposov, S. E. 2018b, *ApJ*, 856, L26  
 Navarrete, C., Chanamé, J., Ramírez, I., et al. 2015, *ApJ*, 808, 103  
 Newberg, H. J., Carlin, J. L. 2015, *Tidal Streams in the Local Group and Beyond*, Springer, New York  
 Norris, J. E., & Da Costa, G. S. 1995, *ApJ*, 447, 680  
 Norris, J. E., Freeman, K. C., & Mighell, K. J. 1996, *ApJ*, 462, 241  
 Norris, J. E., & Ryan, S. G. 1989, *ApJ*, 336, L17  
 Pedregosa, F., Varoquaux, G., Gramfort, A., et al. 2011, *Journal of Machine Learning Research*, 12, 2825  
 Quinn, P. J., & Goodman, J. 1986, *ApJ*, 309, 472  
 Roederer, I. U. 2017, *ApJ*, 835, 23  
 Sanders, J. L., & Binney, J. 2016, *MNRAS*, 457, 2107  
 Sanderson, R. E., Helmi, A., & Hogg, D. W. 2015, *ApJ*, 801, 98  
 Schönrich, R., Binney, J., & Dehnen, W. 2010, *MNRAS*, 403, 1829  
 Slater, C. T., Bell, E. F., Schlafly, E. F. 2014, *ApJ*, 791, 9  
 Suntzeff, N. B., & Kraft, R. P. 1996, *AJ*, 111, 1913  
 Tsuchiya, T., Dinescu, D. I., & Korchagin, V. I. 2003, *ApJ*, 589, L29  
 Tsuchiya, T., Korchagin, V. I., & Dinescu, D. I. 2004, *MNRAS*, 350, 1141  
 Valcarce, A. A. R., & Catelan, M. 2011, *A&A*, 533, A120  
 van den Bosch, F. C., Lewis, G. F., Lake, G., & Stadel, J. 1999, *ApJ*, 515, 50  
 Vasiliev E., 2018, *MNRAS*, in press (arXiv:1802.08239)  
 Veljanoski, J., & Helmi, A. 2018, arXiv:1804.06365  
 Watkins, L. L., Evans, N. W., Belokurov, V., et al. 2009, *MNRAS*, 398, 1757  
 Weinberg, M. D. 1989, *MNRAS*, 239, 549  
 Williams, A. A., & Evans, N. W. 2015, *MNRAS*, 448, 1360  
 Williams, A. A., Belokurov, V., Casey, A. R., & Evans, N. W. 2017, *MNRAS*, 468, 235  
 Wylie-de Boer, E., Freeman, K., & Williams, M. 2010, *AJ*, 139, 636